Soft Matter

ARTICLE TYPE

Cite this: DOI: 00.0000/xxxxxxxxxx

Supplementary Information: On the relationship between cutting and tearing in soft elastic solids

Bingyang Zhang[a] and Shelby B. Hutchens*[a]

Received Date
Accepted Date

DOI: 00.0000/xxxxxxxxxx

Cutting Instrument

Figure S1 shows a photograph of the instrument used for Y-shaped cutting tests. The new configuration, including an increased number of pulleys, enables a more stable cutting phase, a wider available leg angle range, and a larger maximum cutting distance than previously[1]. During testing, the sample is translated down toward the razor blade, which is rigidly mounted on the load cell.

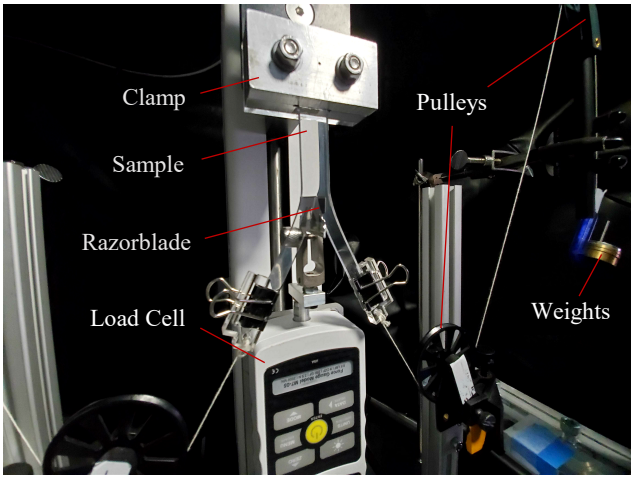

Fig. S1 Test instrument for Y-shaped cutting test. The transparent sample is mounted at the cutting position.

Commercially available razorblades having as-received or manually blunted radii are cleaned prior to cutting tests. Commercial blades include some types used previously:[1] Feather single-edge razorblade (FRB-SE, Feather® Safety Razor, Professional Super), Feather double-edge razorblade (FRB-DE, Feather® Safety Razor), shaving razorblade (SRB, Gillette®, double-edge), utility razorblade (URB, GEM®, single edge, uncoated), and trapezoid utility razorblade (TRB, Stanley®). Manual blunting on URB blades with a large tip radius (BRB) is achieved with an 8000 grit whetstone. Radii (Table S1) are measured via scanning electron microscopy (SEM) and image processing (ImageJ).[1]

Table S1 Measured average radii of selected razorblades

Blade	FRB-SE	FRB-DE	SRB	URB	TRB
R [nm]	38	68	83	129	246
Blade	BRB #1	BRB #2	BRB #3	BRB #4	BRB #5
R [nm]	164	198	221	339	416
Blade	BRB #6	BRB #7	BRB #8	BRB #9	BRB #10
R [nm]	519	560	740	873	989

Cutting and Tearing Contributions

Cutting contributions (C) and tearing contributions (T) of all materials tested are calculated using Eqn. (1) introduced in the main text. These results, together with the corresponding pre-loads (f_{pre}) and the ratios C/T, are listed in Table S2. The T values vary between materials due to the different pre-loads required to reach a designed average pre-stretch $\bar{\lambda} = 1.04 \pm 0.01$. The C values reported in the table correspond to the average threshold cutting energy, G^*_{cut}, in Table 2 of the main text. The thickness for each material is averaged between all samples.

Test Samples for Standard Characterization Methods

Fig. S2 provides schematics of the dogbone-shaped sample used for uniaxial tension tests following ASTM test standards ((ASTM D412-16, die type C)) and the notched sample for pure shear tearing tests. The procedure used to extract tearing energy from pure shear testing are identical to methods listed elsewhere.[1,2] For the uniaxial tension tests, fiducial markers are applied on the surface of the rectangular test region towards the bottom side of the dogbone-shaped sample to match the field of view of the video extensometer. Fig. S2b shows a dog-bone shaped sample pieced together after tensile failure. The simultaneous formation

[a] *Mechanical Science and Engineering, University of Illinois Urbana-Champaign, Urbana, IL, USA.*
* *Tel: 21 7300 0412; E-mail: hutchs@illinois.edu*

Table S2 Pre-loads and cutting and tearing contributions of all materials tested

	Sol-4:1	Sol-1:1	Syl-10:1	Syl-d10:1	UPDMS	BPDMS-80s	BPDMS-90s	BPDMS-95s	BPDMS-98s
f_{pre} [N]	0.98	0.22	0.98	0.25	0.39	0.29	0.34	0.34	0.34
C [J/m^2]	56.2	109.3	45.4	54.4	27.7	11.1	9.8	6.5	8.8
T [J/m^2]	88.5	18.5	87.4	23.0	33.7	27.9	35.0	33.0	32.3
C/T	0.63	5.92	0.52	2.36	0.82	0.40	0.28	0.20	0.27

of cracks at multiple sample locations (red arrows) at the onset of rupture supports the idea that superficial defects were minimized in the polished sample mold.

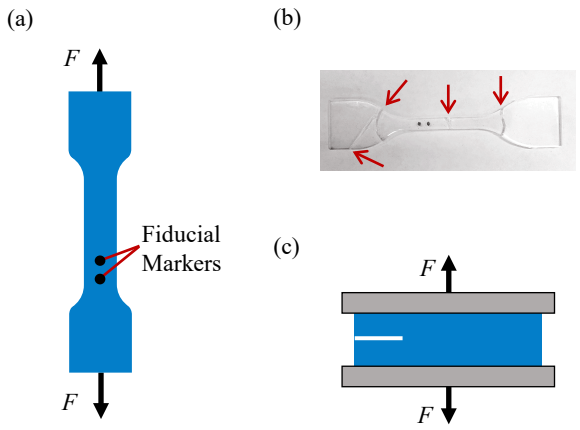

Fig. S2 (a) Illustration of a standard dog-bone shaped sample used for uniaxial tension tests. (b) A post-tensile-failure dog-bone shaped sample. (c) The schematic of a notched sample used for pure shear tearing test.

Modulus Normalized Constitutive Responses

Fig. S3 reproduces the constitutive responses of all materials tested introduced in Fig. 2c of the main text but normalizes the stress responses by the corresponding shear modulus μ determined from the neo-Hookean model for comparison (fit range: $\lambda = 1 - 1.1$, Table 2). Initial linear regions of the constitutive curves cluster under the normalization. In contrast, large-strain nonlinear responses of strong strain-stiffening materials (*e.g.*, Syl-10:1 and Sol-4:1) and very stretchable, more neo-Hookean materials (*e.g.*, Sol-1:1, Syl-d10:1, and UPDMS) are markedly different from the overall linear behaviors of BPDMS (dotted line).

Fit to Arruda-Boyce

We use the approximate form of the incompressible Arruda-Boyce model[3,4] to capture the nonlinear constitutive responses of our selected elastomers. The strain energy density function, using the first five terms of the series expansion form for the inverse Langevin function,[3,4] can be expressed as

$$W = \mu_0 \sum_{i=1}^{5} \alpha_i \frac{1}{\lambda_m^{2i-2}} (I_1^i - 3^i), \tag{S1}$$

where $\alpha_1 = \frac{1}{2}$, $\alpha_2 = \frac{1}{20}$, $\alpha_3 = \frac{11}{1050}$, $\alpha_4 = \frac{19}{7000}$, and $\alpha_5 = \frac{519}{673750}$. μ_0 and λ_m are the two fit parameters. For uniaxial tension, the engineering stress versus stretch relationship is derived from

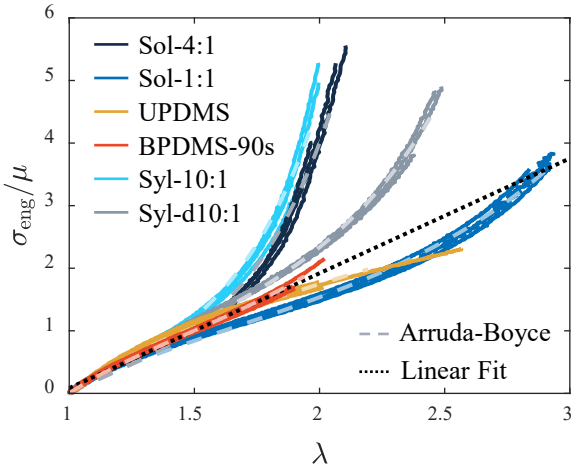

Fig. S3 Shear modulus normalized constitutive responses for all elastomers tested (solid lines). Each Arruda-Boyce fit shown (lighter dashed lines) is averaged between three samples. A linear slope (dotted line) is fit to the curves for BPDMS-90s to demonstrate their nominal linearity.

Eqn. (S1),

$$\sigma_{eng} = 2\mu_0 \left(\lambda - \frac{1}{\lambda^2}\right) \sum_{i=1}^{5} i\alpha_i \frac{1}{\lambda_m^{2i-2}} I_1^{i-1}, \tag{S2}$$

where the first invariant $I_1 = \lambda^2 + \frac{2}{\lambda}$ for uniaxial tension. Fit parameters for all elastomers are listed in Table S3. This approximate form for the Arruda-Boyce model differs from the true Arruda-Boyce model in that the strains can become infinite. In the full Arruda-Boyce model, the strain energy density becomes infinite at sufficiently large, but finite stretch.

Tensile Cycling Test for Syl-10:1

To quantify hysteretic effects, we perform a tensile cycling test for a representative Syl-10:1 material. Fig. S4 shows the engineering stress versus stretch curves at a strain rate of $\sim 0.04\ 1/s$ in consecutive loading-unloading cycles to progressively higher stretches (blue lines of differing color saturation). Minimal hysteresis is observed up to a stretch ≈ 1.5.

Finite Element Analysis (FEA) for Y-Shaped Cutting

FEA for cutting is carried out by simulating hyperelastic cutting indentation at experimental conditions corresponding to cutting within the plateau regime. We model a real-scale, symmetric Y-shaped sample in ABAQUS, as shown in Fig. S5. The displacement and force boundary conditions are applied according to the experimental sample configuration ('XSYMM' symmetry along the center line and fixed y-displacement at the top edge) and preload

Table S3 Fit parameters for the Arruda-Boyce model and the Rubinstein-Panyukov network elasticity model

	Sol-4:1	Sol-1:1	Syl-10:1	Syl-d10:1	UPDMS	BPDMS-80s	BPDMS-90s	BPDMS-95s	BPDMS-98s
μ_0 [MPa]	0.08	0.08	0.09	0.06	0.17	0.37	0.33	0.30	0.32
λ_m	1.0	2.1	1.0	1.6	596.5	1.9	1.7	1.6	1.6
E_x [MPa]	1.12	0.16	1.20	0.27	0.54	1.42	1.30	1.33	1.36
E_e [MPa]	3×10^{-8}	0.2	2×10^{-14}	4×10^{-11}	1×10^{-2}	4×10^{-8}	9×10^{-2}	3×10^{-7}	4×10^{-7}
$\langle r_0\rangle$ [nm]	5.51	14.76	5.31	11.13	7.92	4.89	5.11	5.05	5.00

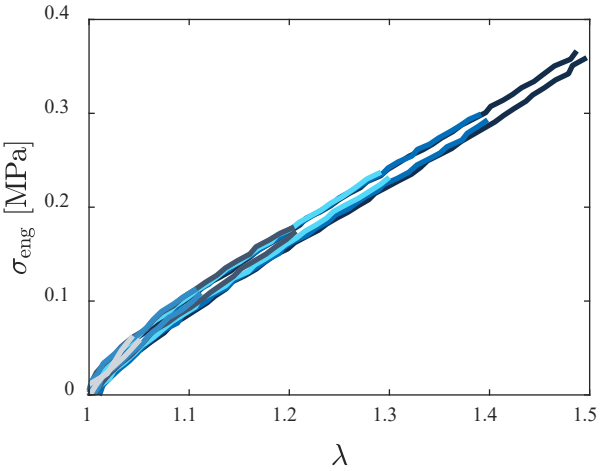

Fig. S4 Engineering stress versus stretch response of Syl-10:1 in consecutive tensile cycles (strain rate: $\sim 0.04\ 1/s$). Changes in the blue color saturation indicate different load-unload cycles.

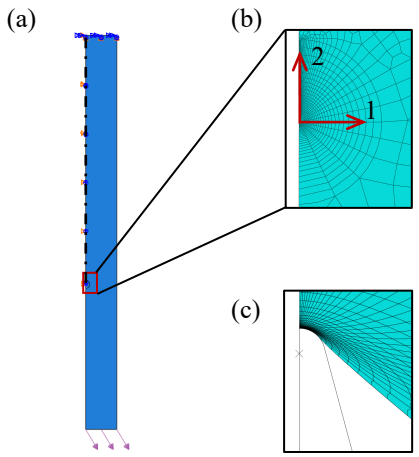

Fig. S5 Illustrated FE model and meshing for Y-shaped cutting. (a) A real-scale symmetric model for a Y-shaped sample. A 'XSYMM' boundary condition is applied to the upper part of the body (black dash-dotted line). A preload matching the experimental condition is applied to the lower leg in the form of surface traction. (b) A close-up image of the circular partition and the gradient meshing near the crack tip. The local coordinate system is labeled in red arrows. (c) Elastic contact between the sample and a rigid blade surface, after the preload is applied.

forces, respectively (Fig. S5a). Eight-node quadrilateral plane-stress elements (CPS8) are selected. A circular fine mesh zone of a radius ~1 mm partitions the near-crack-tip region. The fine mesh zone uses a size gradient that increases radially away from the crack tip ($\approx 1\times10^{-6} - 1\times10^{-2}$ mm)(Fig. S5b). This fine mesh accommodates the local large strain/stress concentration applied by the blade. Following the application of preloads, a rigid analytical surface having the same dimensions as a sharp razorblade contacts the sample surface at the notch vertex under a 'frictionless' condition (Fig. S5c). A controlled longitudinal displacement produces a reaction force history that is used to determine simulation loading conditions of interest corresponding to the experimental conditions for steady-state cutting within the plateau regime. The deformation fields are then extracted from the deformed configuration.

The Effect of Blade Tip Radius on FE Asymptotic Fields

To demonstrate the negligible effect of blade radius on the stress field at a length scale $r > \sim 3\times10^{-4}$ mm (Section 3.2 of the manuscript), thus allowing blade contact to be treated as a line load on a hyperelastic half space (nonlinear Flamant problem), we compare the FE results for Y-shaped cutting at the same cutting force but two different blade radii ($R \approx 130$ nm and $R \approx 725$ nm). The asymptotic stress and strain components (σ_{11}, σ_{22}, λ_{11}, and λ_{22},) are obtained along the center line of a simulated Syl-10:1 sample as functions of the distance from the crack tip, r (Fig. S6). The same reaction force conditions, corresponding to the experimental cutting force within the plateau regime (~ 0.13 N), are implemented for both radii. It is evident that the near-tip asymptotic fields become blade-radius-independent outside a length scale $r \sim 3\times10^{-4}$ mm, which is in the order of magnitude of a typical blade radius used.

Interpretation of FE Results Far from the Crack Tip

In Figs. 3a and 3b, as $r\to\infty$, $\sigma_{11}\to 0$ and σ_{22} tends toward a small but finite tensile value that differs slightly between the material formulations. The latter arises from experimental conditions due to differences in the threshold cutting force between materials. Under plane stress constraints, the application of pre-loads at a given angle in the two legs produces bending moments that must be supported in the wider leg about 1 mm from the crack tip. In reality, these small moments probably cancel one another nearer the crack tip through slight sample twist. This constraint gives rise to the short-region of low magnitude compressive stress in σ_{11} (lighter symbols, Fig. 3a for increasing r. For the same reason, σ_{22} exhibits an unnaturally sharp transition to the far-field value in the same $r = 1-10$ mm region.

FEA for Nonlinear Flamant Problem

A FE simulation for a line load acting on a hyperelastic Arruda-Boyce half space, *i.e.*, the nonlinear Flamant problem, is carried out to verify the associated asymptotic stress fields. As shown in

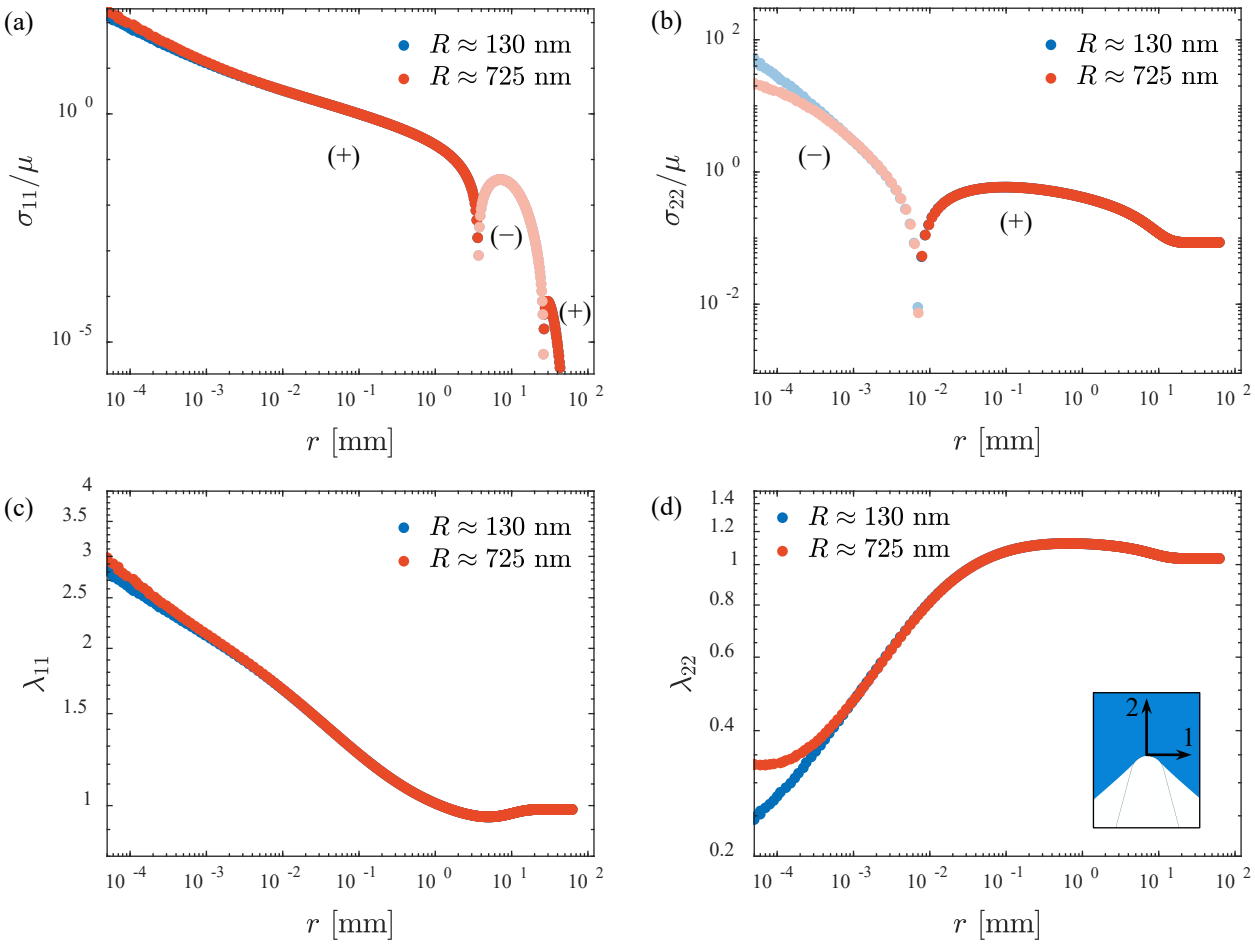

Fig. S6 FE asymptotic stress and stretch components for a Syl-10:1 material at two different blade radii ($R \approx 130$ nm, orange data points and $R \approx 725$ nm, blue data points). The magnitude of the stresses normalized by the shear modulus is marked with $(+)$ for tension (saturated points) and $(-)$ for compression (light-colored points). (a) Normalized crack-opening stresses (σ_{11}) along the sample center line. (b) Normalized longitudinal stresses (σ_{22}) along the sample center line. (c) Crack-opening stretches (λ_{11}) along the sample center line. (d) Longitudinal stretches (λ_{22}) along the sample center line. Inset: Illustration of a blade-sample contact with the local coordinate system.

Fig. S7, a unit line load, $F = 1$, compresses a strain-stiffening substrate material having constitutive parameters of Syl-10:1. The transverse stresses σ_{11} and the longitudinal stresses σ_{22} are extracted along the vertical line of load from the deformed configuration. We compare σ_{11} and σ_{22} to a $1/r$ singularity (light-colored dotted lines) within ranges $r = 10^{-3} - 5 \times 10^{-2}$ mm and $r = 10^{-3} - 10^{-1}$ mm, respectively. The results show that both asymptotic stress components deviate little from a $1/r$ singularity near the crack tip. This simulation for the nonlinear Flamant problem agrees with the theoretical predictions in literature.[5]

FE Analysis of A Minimum Damage Zone from Blade Indentation

As discussed in Section 4.2 of the manuscript, We perform FE simulation of a blade indenting a hyperelastic Arruda-Boyce half-plane to determine the radius-normalized damage volume $V/(R^2 t)$ and its dependence on modulus-normalized applied force per unit thickness $F/(\mu R)$. As illustrated in Fig. S8, a rigid blade surface having a unit radius indents elastically into a material substrate (CPS8 plane-stress quadrilateral elements) with controlled displacements. The contact simulation in Abaqus adopts a 'hard contact' normal behavior to minimize the penetration of the slave surface and a 'frictionless' tangential behavior to be consistent with experimental cutting conditions. Reaction forces per thickness F in the direction of indentation are extracted at increasing displacements. The corresponding damage volumes V are calculated at the same time from the sum of the volumes of all elements that satisfy a given modulus-normalized strain energy density threshold, w_t/μ. As demonstrated in Fig. S8, the resultant $V/(R^2 t)$ vs. $F/(\mu R)$ curves shift positive or negative depending on the w_t/μ threshold. The desired w_t/μ is obtained when a reference point (closed symbol, marked by orange dotted lines) at $V/(R^2 t) = V_{\min}/(L^{*2} t) = 4$ is equal to a normalized force $F/(\mu R) = F/(\mu L^*)$ that matches the experimental cutting force within the plateau regime.

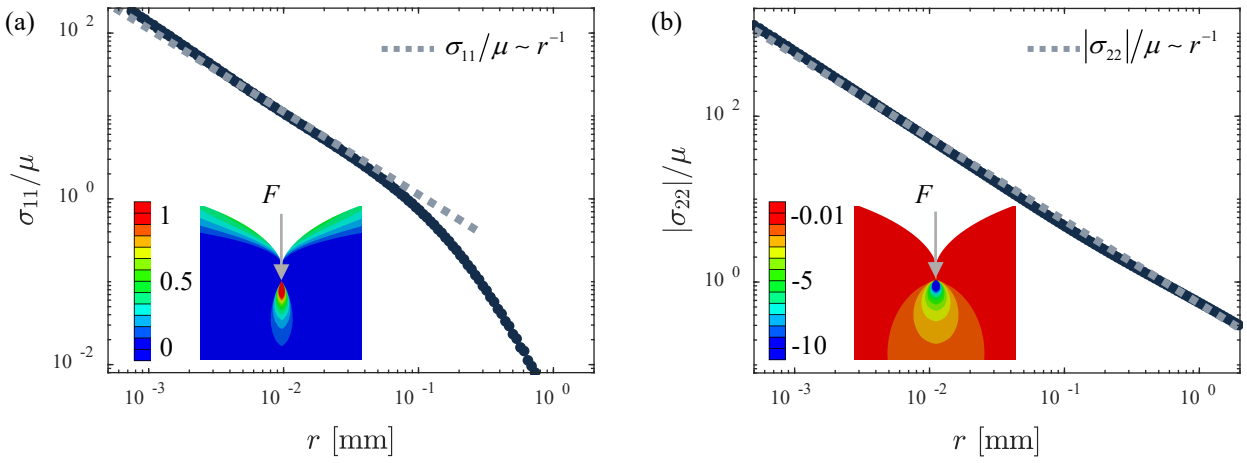

Fig. S7 Simulated stress components for the nonlinear Flamant problem. (a) Shear modulus μ normalized transverse stresses σ_{11} compared with a $1/r$ singularity (light-colored dotted line) along the vertical line of load. The inset shows a contour plot of the asymptotic stress field. (b) Normalized longitudinal stress magnitudes $|\sigma_{22}|/\mu$ agree with a $1/r$ singularity over three decades.

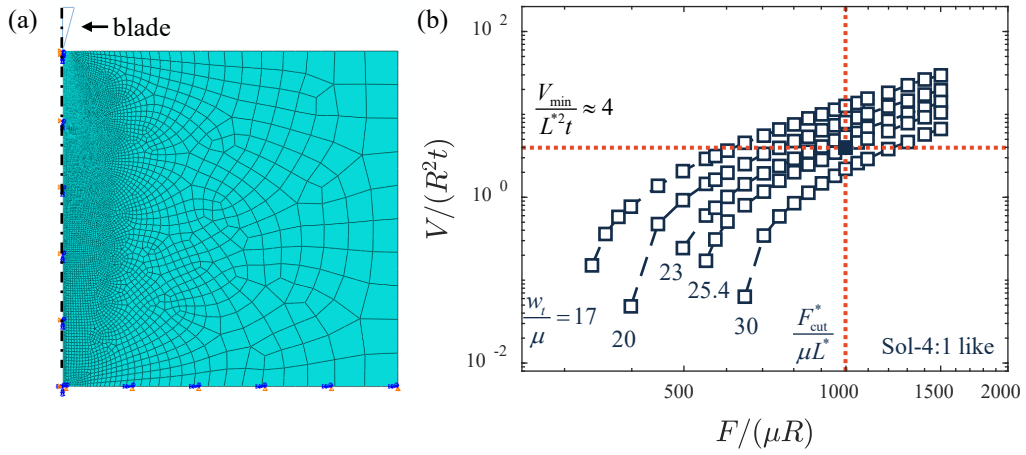

Fig. S8 FE Characterization of a minimum damage zone using blade indentation on a hyperelastic half space. (a) The FE meshing and test configuration. The plane of symmetry is marked by the dash-dotted line. A 'YSYMM' boundary condition is applied for the bottom surface of the half space. (b) The $V/(R^2t)$ vs. $F/(\mu R)$ curve shifts positive or negative at different threshold w/μ values. The best threshold $w/\mu \approx 25.4$ is determined through tuning when $V/(R^2t) = V_{\min}/(L^{*2}t) = 4$ at an experimental cutting force $F/(\mu R) = F/(muL^*)$.

A Network Elasticity Model to Determine Crosslink Density for the Lake and Thomas Model

To determine the contribution of crosslinks and entanglements in our materials, we fit the uniaxial stress-stretch data with the network elasticity model proposed by Rubinstein and Panyukov[6,7]

$$\sigma = \frac{1}{3}\left(\lambda - \frac{1}{\lambda^2}\right)\left(E_x + \frac{E_e}{0.74\lambda + 0.61\lambda^{-0.5} - 0.35}\right), \tag{S3}$$

where E_x and E_e are the contribution of crosslinks and entanglements, respectively. Fitting curves and fitting parameters for a stretch range $\lambda = 1 - 1.5$ are shown in Fig. S9 and Table S3, respectively. The average number of backbone bonds N_x is then estimated from E_x

$$N_x = \frac{3\rho N_A k_B T}{M_0 E_x}, \tag{S4}$$

where ρ is the material density, N_A is the Avogadro's constant, k_B is the Boltzmann constant, T is the absolute temperature, and $M_0 = 37$ g/mol is the average molecular weight of a PDMS backbone atom. The bulk density of crosslinks ν_x is determined by the relationship $E_x = 3\nu_x k_B T$. The average distance between crosslinks $\langle r_0 \rangle$ is calculated via the expression $\langle r_0 \rangle = l_0\sqrt{C_\infty N_x}$, as mentioned in the main text. The resultant $\langle r_0 \rangle$ values for all materials tested are provided in Table S3.

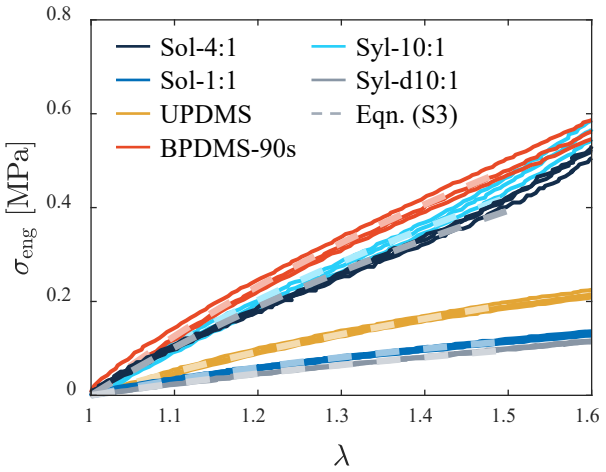

Fig. S9 Fitting results for the network elasticity model. Constitutive responses of elastomers (solid lines) are fit within a stretch range $\lambda = 1 - 1.5$ (light-colored dashed lines).

Estimating Enthalpic Distortion of PDMS from Single-Strand Stretch Data

We estimate a more accurate released energy U for chain breakage from single-strand stretch data described by the modified freely jointed chain model (m-FJC) following the work of Wang et al.[8] A good approximation of U is given by the associated enthalpic distortion energy per bond, U_e, which has a form[8]

$$U \approx U_e = \frac{1}{2}\frac{f_b^2}{f_s} l_0. \tag{S5}$$

The characteristic stretching force f_s can be calculated from

$$f_s = k_{\text{Kuhn}} b \tag{S6}$$

We estimate the Kuhn segment stiffness k_{Kuhn} and the Kuhn length b by fitting experimental force versus extension data for a single PDMS strand from literature[9] with the m-FJC model, which takes a form[8,10]

$$R = L_0\left[\coth\left(\frac{fb}{k_B T}\right) - \frac{k_B T}{fb}\right]\left(1 + \frac{f}{k_{\text{Kuhn}} b}\right), \tag{S7}$$

where R is the average end-to-end distance, L_0 is the contour length, and f is the tension. The best fitting result is shown in Fig. S10 (red dashed line), which gives $k_{\text{Kuhn}} \approx 12.9$ N/m and $b \approx 1.47$ nm, yielding $U \approx U_e \approx 4.89 \times 10^{-20}$ J. We note that the order of magnitude of the estimated U agrees with an estimation predicted using the wormlike chain model (WLC) and an average persistence length $p \approx 0.31$ nm.[9] The force on a single polymer chain according to the WLC model can be written as[10]

$$f = \frac{k_B T}{p}\left[\frac{1}{4}\left(1 - \frac{R}{L_0}\right)^{-2} + \frac{R}{L_0} - \frac{1}{4}\right] \tag{S8}$$

For a typical number of backbone atoms $N = 465$ and a Si-O bond length 0.165 nm,[11] the area under the curve of the WLC model predicts $U \approx 1.7 \times 10^{-20}$ J, close to the estimate obtained from Eqn. (S5) despite its being a more simplified model.

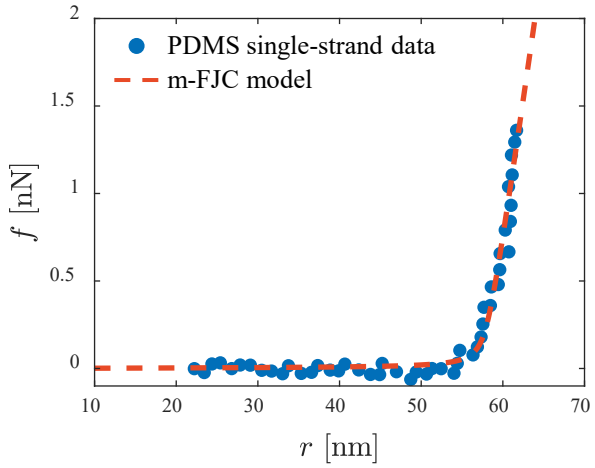

Fig. S10 PDMS single-strand stretch data[9] (blue circles) fit with the m-FJC model (red dashed line)

Mechanical and Fracture Responses of Bimodal PDMS Networks

We use the BPDMS system as a controlled model material for some of the findings discussed in the main text, including mapping cutting and tearing and the existence and onset of the plateau and the strain-stiffening responses in cutting. With the BPDMS materials, we create an elastomer with a designed constitutive response by changing only two network components. The mechanical performance of the BPDMS depends on its specific chemical compositions. Particularly, short chains bear stresses via their finite extensibility induced strain-stiffening, while long

chains provide high stretchability. This creates a toughening mechanism that may explain why the constitutive responses of BPDMS in Fig. 2 show slightly reduced stretchability but comparable or even larger tensile strength compared to the UPDMS counterpart (e.g., BPDMS-90s vs. UPDMS). The chain-mediated mechanical behaviors also enable systematic control over the constitutive response of BPDMS. As introduced in the Materials Section of the manuscript, the BDPMS networks are comprised of a long-chain with molecular weight M_l and a 500 g/mol molecular weight short-chain at a concentration m_s. The m_s values are tuned according to the corresponding M_l to produce identical nonlinear stress vs. stretch response, but lead to different ultimate properties. We verify the controlled nonlinear elastic response via the uniaxial tests shown in Fig. 2d. The constitutive curves coincide with each other within their extensibility. The maximum relative difference is less than 5%. At the same time, ultimate properties differ between BPDMS, namely λ_b and w_b decrease with the increasing m_s — with the exception of BPDMS-80s. This trend is anticipated from previous experimental observations[12,13] and may only apply when the increment of stretchability due to the increased long-chain length does not compensate for the brittleness caused by the increased short-chain concentration.

At the short chain concentrations used, BPDMS is thought to exhibit architectural inhomogeneity in the BDPMS, theorized to originate from kinetics-driven short-chain clustering.[14–18] The onset of short-chain clustering/aggregation occurs when the probability of end-linking short chains becomes much higher than end-linking long chains in a pre-polymer mixture. Therefore, forming a heterogeneous structure of short chain clusters linked by longer chains requires both a high short-chain concentration and a large difference between the two chain lengths. It has been suggested in some bimodal PDMS networks[15,18] that a threshold short-chain concentration may exist below which the short-chain clustering likely vanishes and the network becomes homogeneous. We speculate that the short-chain molar concentration of BPDMS-80s is approaching such a threshold as we observe a reduction in its cutting energy and strain at failure after all previous formulations with decreasing short chain concentration were increasing in these properties. Such short-chain clustering may result in 'super-crosslink' structures linked by long chains with a relatively high effective coordination number (>4). These structures have been suggested as serving as topological restraints that are responsible for the stiffening and toughening effects observed in bimodal networks compared to their unimodal counterparts[14,18,19]. For example, BPDMS-90s appears to have both higher μ and w_b than UPDMS, and a comparable G_{tear} despite the fact that BPDMS-90s has a much smaller average end-to-end distance between crosslinks than UPDMS.

Notes and references

1 B. Zhang, C. S. Shiang, S. J. Yang and S. B. Hutchens, *Experimental Mechanics*, 2019, 517–529.

2 J.-Y. Sun, X. Zhao, W. R. K. Illeperuma, O. Chaudhuri, K. H. Oh, D. J. Mooney, J. J. Vlassak and Z. Suo, *Nature*, 2012, **489**, 133–136.

3 E. M. Arruda and M. C. Boyce, *Journal of the Mechanics and Physics of Solids*, 1993, **41**, 389–412.

4 M. C. Boyce, *Rubber Chemistry and Technology*, 1996, **69**, 781–785.

5 V. M. Mal'kov and Y. V. Mal'kova, *Journal of Applied Mathematics and Mechanics*, 2008, **72**, 468–474.

6 M. Rubinstein and S. Panyukov, *Macromolecules*, 2002, **35**, 6670–6686.

7 J. Slootman, V. Waltz, C. J. Yeh, C. Baumann, R. Göstl, J. Comtet and C. Creton, *Physical Review X*, 2020, **10**, 41045.

8 S. Wang, S. Panyukov, M. Rubinstein and S. L. Craig, *Macromolecules*, 2019, **52**, 2772–2777.

9 S. Al-Maawali, J. E. Bemis, B. B. Akhremitchev, R. Leecharoen, B. G. Janesko and G. C. Walker, *Journal of Physical Chemistry B*, 2001, **105**, 3965–3971.

10 M. I. Giannotti and G. J. Vancso, *ChemPhysChem*, 2007, **8**, 2290–2307.

11 Alex C. M. Kuo, *Polymer Data Handbook*, Oxford University Press, Inc., 1999, pp. 411–435.

12 J. E. Mark, *Accounts of Chemical Research*, 1994, **27**, 271–278.

13 M. A. Llorente, A. L. Andrady and J. E. Mark, *Journal of polymer science. Part A-2, Polymer physics*, 1981, **19**, 621–630.

14 B. D. Viers and J. E. Mark, *Journal of Macromolecular Science, Part A: Pure and Applied Chemistry*, 2007, **44**, 131–138.

15 F. B. Madsen, A. E. Daugaard, C. Fleury, S. Hvilsted and A. L. Skov, *RSC Adv.*, 2014, **4**, 6939–6945.

16 W. Michalke, S. Kreitmeier, M. Lang, A. Buchner and D. Göritz, *Computational and Theoretical Polymer Science*, 2001, **11**, 459–466.

17 H. Oikawa, *Polymer*, 1992, **33**, 1116–1119.

18 G. D. Genesky, B. M. Aguilera-Mercado, D. M. Bhawe, F. A. Escobedo and C. Cohen, *Macromolecules*, 2008, **41**, 8231–8241.

19 G. B. Shah, *Journal of Applied Polymer Science*, 2004, **94**, 1719–1722.